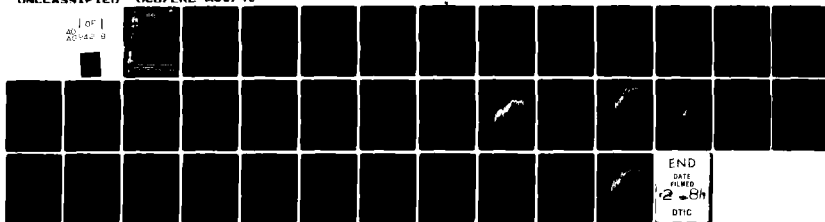


AD-A094 289

CALIFORNIA UNIV BERKELEY ELECTRONICS RESEARCH LAB F/8 12/1
LOWER-HYBRID DRIFT INSTABILITY SATURATION MECHANISMS IN ONE-DIM--ETC(U)
SEP 80 Y - CHEN, C K BIRDSALL N00014-77-C-0578
UNCLASSIFIED UCR/FRL-M80/40 NL

1 OF 1
AD-A094 289



END
DATE
FILMED
2-84
DTIC

12

LEVEL

LOWER-HYBRID DRIFT INSTABILITY SATURATION
MECHANISMS IN ONE-DIMENSIONAL SIMULATIONS

by

Y.-J. Chen and C. K. Birdsall

DTIC

JAN 29 1981

Memorandum No. UCB/ERL M80/40

19 September 1980

DISTRIBUTION STATEMENT A

Approved for public release;
Distribution Unlimited

ELECTRONICS RESEARCH LABORATORY
College of Engineering
University of California, Berkeley, CA 94720
80 12 15 150

127 550

AD A094289

DOC FILE COPY 1-3-81

(12)

(6) LOWER-HYBRID DRIFT INSTABILITY SATURATION MECHANISMS
IN ONE-DIMENSIONAL SIMULATIONS.

by

(10) Y.-J. Chen and C. K. Birdsall

DTIC
UNCLASSIFIED

14
Memorandum No. UCB/ERL-M80/40

(11) 19 Sep 1980

(15) N44-77-2-1516

continued F.14

ELECTRONICS RESEARCH LABORATORY

College of Engineering
University of California, Berkeley
94720

DISTRIBUTION STATEMENT A
Approved for public release;
Distribution Unlimited

550

LOWER-HYBRID DRIFT INSTABILITY SATURATION MECHANISMS IN ONE-DIMENSIONAL SIMULATIONS

Yu-Juan Chen and C.K. Birdsall

Electronics Research Laboratory

University of California, Berkeley, CA. 94720

ABSTRACT

The linear properties and saturation mechanisms of the lower-hybrid drift instability have been investigated using a one-dimensional particle-hybrid simulation. For low drift velocities ($v_d \ll v_{te}$), ion trapping and current relaxation ($v_d \rightarrow 0$) are competing processes for stabilization. If the relative electron-ion drift velocity is kept constant in time, ion trapping causes the end of instability growth; if this drift is allowed to decrease consistent with momentum balance, then saturation is due to current relaxation.

September 19, 1980

V. pub. d. m. e. f. 7/11

Accession For	
NTIS GRA&I	<input checked="" type="checkbox"/>
DTIC TAB	<input type="checkbox"/>
Unannounced	<input type="checkbox"/>
Justification	<i>for file</i>
By	
Distribution/	
Availability Codes	
Dist	Special
A	

LOWER-HYBRID DRIFT INSTABILITY SATURATION MECHANISMS IN ONE-DIMENSIONAL SIMULATIONS

Yu-Juan Chen and C.K. Birdsall

Electronics Research Laboratory

University of California, Berkeley, CA. 94720

I. INTRODUCTION

The lower-hybrid drift instability¹ may play an important role in the dynamics of plasma experiments, such as θ -pinches and field-reversed configurations. According to the linear theory and experiments, during the implosion phase of a theta-pinch this instability is responsible for the flute observed in the current sheath region²⁻⁴. Two dimensional particle simulations of this instability with a finite plasma beta value for large drift velocities were performed by Winske and Liewer⁵. During the post-implosion phase, it is considered to be the dominant instability^{6,7}. If this instability saturates at high levels, it will contribute to anomalous transport, and influence the resistivity, for example. Saturation mechanisms of the lower-hybrid drift instability during the post-implosion phase is the main concern of this paper.

In the post-implosion region, the difference of the cross-field velocity, $v_d = v_{de} - v_{di}$, is less than the ion thermal velocity, $v_{ti} = (T/m_i)^{1/2}$. Anomalous transport coefficients in this region were derived from quasilinear theory^{7,8}. For low-beta plasmas, Davidson⁸ predicted that current relaxation ($v_d \rightarrow 0$.) and plateau formation ($\partial f_i / \partial v_i \rightarrow 0$.) in the ion velocity distribution are generally competing processes for stabilization. If the initial drift velocity v_d is very small, then it is energetically favorable for stabilization to occur through formation of the plateau. Otherwise, plateau formation will not have been completed when the cross-field current relaxes to zero. Electron resonance broadening has also been considered as a possible satura-

tion mechanism for high-beta plasmas^{9,10}.

In this paper, one-dimensional particle-hybrid simulation studies of the lower-hybrid drift instability are presented. Our simulation model is a slab with a constant density gradient; the ions are unmagnetized particles, shielded by strongly magnetized electrons through the linear electron charge density susceptibility, χ_e . Ions are initially in a steady equilibrium state with the ion diamagnetic drift velocity cancelled by the $\vec{E} \times \vec{B}$ drift, corresponding to electrostatically confined ions. At small amplitudes, our simulations show good agreement with linear theory, such as the linear growth rate, the mode frequency, and the influence of finite beta effects associated with the nonresonant ∇B_e electron orbit modifications¹¹⁻¹³. Ignoring effects of finite beta, it is found that the end of wave growth is due to ion trapping when both the density gradient and the cross-field current velocity v_d are kept constant in time. When v_d is allowed to vary in time, our simulations show that stabilization of the wave occurs through current relaxation.

In Section II.A, a brief review of the linear theory of the lower-hybrid drift instability is given. A description of the simulation method is presented in Section II.B. We solve the linear dispersion relation of our simulation model (with a multibeaming system) numerically. Comparisons of observed linear properties of the growing waves with linear theory are made and given in Section III. Investigation of various saturation processes is presented in Section IV. At low drift velocities, ion trapping causes the end of wave growth when drift velocities are kept constant in time. It is found that the saturation level predicted by quasilinear theory is the saturation level of the most unstable mode for ion trapping. A detailed explanation is given in Section III.A. An analytic formula for the saturated field energy spectrum in k space for ion trapping when $v_d \ll v_e$ is derived. Section III.B is devoted to a description of how current relaxation can stabilize the instability. The simulation method for allowing v_d to vary in time is also described. Simulated saturation levels agree fairly well with the predictions of quasilinear theory. Conclusions are given in Section V.

II. LINEAR THEORY AND SIMULATION MODEL

A. Review of Linear Theory

Our model is a slab with a constant density gradient in the y direction (Fig. 1). The electron drift across the magnetic field $B_0 \hat{z}$ with mean fluid velocity

$$v_{\perp} = v_I + v_e \quad (1)$$

where v_I is the $\vec{E} \times \vec{B}$ drift velocity, and

$$v_e = -\frac{T_e}{m_e \omega_{ce}} \frac{\partial}{\partial y} \ln(n_e) \quad (2)$$

is the electron diamagnetic drift velocity, ω_{ce} is the electron cyclotron frequency, m_e is the electron mass, T_e is the electron temperature and $n(y) = n_e \approx n_i$ is the density. There is no net ion current in the x direction, i.e.,

$$v_{\perp} = v_I + v_i = 0, \quad (3)$$

which is a consequence of the ion pressure force being balanced by the ambipolar electric force in the y direction. v_i is the ion diamagnetic drift velocity as given

$$v_i = \frac{T_i}{m_i \omega_{ci}} \frac{\partial}{\partial y} \ln n_i, \quad (4)$$

where T_i , m_i , ω_{ci} are the ion temperature, mass and cyclotron frequency, respectively. The electrostatic simulations were performed with \vec{E}_1 and displacement only in the x direction.

The lower-hybrid drift instability is characterized by strongly magnetized cold electrons and unmagnetized hot ions with

$$\begin{aligned} \omega &\ll \left| \omega_{ci} + i\gamma \right| \ll \omega_{ce}, \\ k^2 a_i^2 &\gg 1, \quad k^2 a_e^2 \leq 1, \\ T_i &\gg T_e. \end{aligned} \quad (5)$$

With these inequalities, the dielectric function for cold electrons and Maxwellian ions is expressed as

$$\begin{aligned} D(k, \omega) &= D_R(k, \omega) + iD_I(k, \omega) \\ &= 1 + \frac{\omega_{pe}^2}{\omega^2} + \frac{1}{k^2 \lambda_{Di}^2} \frac{\omega}{\omega - kv_I} + i\sqrt{\frac{\pi}{2}} \frac{1}{k^2 \lambda_{Di}^2} \frac{\omega}{|k|v_i} \end{aligned} \quad (6)$$

The real part of the frequency is determined to zeroth order in $\left| \frac{\gamma}{\omega} \right| \ll 1$ by

$$D_R(k, \omega_r) = 1 + \frac{\omega_{pe}^2}{\omega_{ci}^2} + \frac{1}{k^2 \lambda_D^2} \cdot \frac{\omega_r}{\omega_r - k v_T} = 0 \quad (7)$$

The solution is

$$\omega_r = \frac{k^2}{k^2 + k_m^2} k v_T \equiv \omega_{ur} \quad (8)$$

The growth rate, $\gamma = -D_I / (\partial D_R / \partial \omega)_{ur}$, is given by

$$\gamma = \sqrt{\frac{\pi}{2}} \frac{k^2 / k_m^2}{(1 + k^2 / k_m^2)^{3/2}} \left| \frac{k}{k_m} \right| \left(\frac{v_T}{v_i} \right)^2 \omega_{ur} \quad (9)$$

where

$$k_m^2 = \frac{1}{\lambda_D^2} \cdot \frac{1}{1 + \omega_{pe}^2 / \omega_{ci}^2} = \omega_{lh}^2 / v_i^2 \quad (10)$$

is the wave number of the most unstable mode, and

$$\omega_{lh} = \frac{\omega_m}{\sqrt{1 + \omega_{pe}^2 / \omega_{ci}^2}} \quad (11)$$

is the lower hybrid frequency.

B. Simulation Method and Linear Dispersion

In our simulation, the ions are unmagnetized, fully nonlinear, and modeled by particles. The relative electron-ion drift velocity v_d is $v_d = v_{de} - v_{di} \approx v_T$ when $T_e \gg T_i$. Electrons were represented as a warm fluid with linear susceptibility $\chi_e(k, \omega)$ which is given by

$$\chi_e(k, \omega) = \frac{\omega_{pe}^2}{\omega_{ci}^2} \cdot \frac{1 - I_0(b) e^{-b}}{b} + \frac{\omega_{pe}^2}{k^2 v_i^2} \cdot \frac{k \cdot v_T(k)}{\omega - k v_T} \quad (13)$$

from the local theory, where

$$\begin{aligned} b &= k^2 \frac{T_e}{m_e \omega_{ci}^2} \quad , \\ v_T(k) &= - \frac{T_e}{m_e \omega_{ci}^2} I_0(b) e^{-b} \\ &\quad \times \left\{ \frac{\partial}{\partial v} \ln n - \frac{\partial}{\partial v} \ln B \left[1 - b \left(1 - \frac{I_1(b)}{I_0(b)} \right) \right] - \frac{\partial}{\partial v} \ln T_e \cdot b \left(1 - \frac{I_1(b)}{I_0(b)} \right) \right\} \quad (14) \end{aligned}$$

$I_n(b)$ is the modified Bessel function of the first kind of order n . The 1d Fourier transformed

Poisson equation,

$$\left[1 + \chi_e(k, \omega) \right] \phi_k(t) = \frac{4\pi}{k^2} \rho_k(t), \quad (15)$$

may be written as

$$\begin{aligned} \left[1 + \left(\frac{\omega_{pe}}{\omega_{ce}} \right)^2 \frac{1 - I_0(b) e^{-b}}{b} \right] \left(i \frac{\partial}{\partial t} - k v_E \right) \phi_k(t) \\ + \frac{\omega_{pe}^2}{k^2 v_{te}^2} k v_{*}(k) \phi_k(t) = \frac{4\pi}{k^2} \left(i \frac{\partial}{\partial t} - k v_E \right) \rho_k(t) \end{aligned} \quad (16)$$

by replacing ω with the operator $i \frac{\partial}{\partial t}$. Eq. (16) was used to advance $\phi_k(t)$. Similar one-dimensional hybrid simulations for the drift-cyclotron instability have been carried out by Cohen et al.^{14,15}

Quasilinear theory^{7,8} predicts that the field fluctuations of the lower-hybrid drift instability saturate at a very low level compared with the thermal energy for $v_d \ll v_{te}$. In order to observe growth in the linear regime in our simulation, it was decided to load particles orderly in phase space (quiet start), with a Maxwellian distribution, in order to reduce the initial fluctuation level. However, the quiet start Maxwellian consists of many discrete beams which can produce multibeam instability as pointed out by Dawson¹⁶; hence, we needed to analyze the normal modes, of the ion beams and the cold electrons with χ_e from Eq. (13).

The ion susceptibility, χ_i , is obtained from applying the linearized fluid equation of motion and equation of continuity to each ion beam of zero order drift velocity V_i and density N_i , with the well known result, for one ion beam

$$\chi_i = - \frac{4\pi N_i e^2}{m_i (\omega - k V_i)^2}. \quad (17)$$

The dielectric function is $D(k, \omega) = 1 + \chi_e + \chi_i$, so that the dispersion relation $D=0$ for many ion beam is,

$$1 + \chi_e = \sum_i \frac{4\pi N_i e^2}{m_i} \frac{1}{(\omega - k V_i)^2}. \quad (18)$$

The dispersion relation was solved numerically by using the solver supplied by Au-Yeung and Friedman¹⁷. It is found that there are two kinds of modes in the system: the lower-hybrid

drift wave with dispersion affected very little by the discrete beams; and the multibeam instability with growth rate comparable to that of the lower-hybrid drift instability. In Fig. 2 dispersion curves are plotted for the lower- hybrid drift mode and the fastest growing multibeaming mode with parameters:

$$N = N_b = 16384 ,$$

$$m_i/m_e = 1600.,$$

$$\omega_{pe}^2/\omega_{pi}^2 = 1,$$

$$\lambda_D/\Delta x = 1.44 ,$$

$$v_I/v_e = 0.424263,$$

$$T_i = 0 ,$$

$$L_n/L_B = 0, \text{ and}$$

$$L_n/L_I = 0 .$$

$L_n = 1/(\partial \ln n / \partial y)$, $L_B = 1/(\partial \ln B_o / \partial y)$, and $L_I = 1/(\partial \ln T / \partial y)$ are the scale lengths of the density, magnetic field and temperature, respectively. N_b is the number of beams, which was taken as the number of particles because in the quiet start Maxwellian loading, each particle was given a different velocity, in order to minimize the multi-beaming instability.

III. SIMULATION RESULTS AT LINEAR STAGE

The corresponding simulation results for the mode number $M = 5$ are shown in Fig. 3 (the mode energy history plot) and Fig. 4 (the power spectrum vs. frequency plot at various times), where the mode number M is defined as $M = kL / 2\pi$. Typical parameters used are the number of spatial grids $NG = 64$, the time step $\omega_{pi} \Delta T = 0.2$, the length $L = 44.43 \lambda_D$. All the results presented in this section are from single mode simulation, i.e., only one Fourier component of electric potential was used to push ion particles. Figure 4 shows a well defined lower-hybrid drift frequency at $\omega/\omega_{pi} \approx 0.136$ as well as many multibeam mode frequencies. As time goes on, the lower-hybrid drift wave grows faster than the multibeam modes do, and eventually becomes dominant. We measured the lower-hybrid drift mode peak values at different times, and calculated its linear growth rate. The simulation frequencies and growth rates are shown in Fig. 2; they agree with the prediction very well.

In general, the growth rate for a given mode number M increases as v_T/v_{th} increases. Figure 5 presents mode energy history plots for (a) $v_T/v_{th} = 0.57$ and (b) 0.85, respectively. The growth rates can be easily measured from the slopes of Figs. 5a and 5b. The dependence of the linear mode frequency observed in the simulation on v_T/v_{th} and comparison of these results with linear theory (Eq. 18) for the mode number $M=5$ are given in Fig. 6. Mode 5 is approximately the most unstable mode for the parameters we used.

The addition of finite beta alters the growth rates. The beta value is given by $\beta = -2L_n/L_R$ as $T_e = 0$. In Fig. 7, dispersion curves are plotted for $v_T/v_{th} = 1.1314$, ((a) $L_n/L_R = 0$, and (b) $L_n/L_R = -0.40$ where the negative sign means the gradients of density and magnetic field have opposite directions. Figure 8 gives dispersion curves for $v_T/v_{th} = 1.5556$, (a) $L_n/L_R = 0$, and (b) $L_n/L_R = -0.36$. Figs. 7 and 8 show that the lower-hybrid drift waves at small mode number M are stabilized by the finite beta effects associated with the nonresonant ∇B_{\perp} electron orbit modification (the term-proportional to $(\mathbf{1} \cdot \mathbf{B}_{\perp})(\partial B_{\perp}/\partial y)$ in Eq. (6)) as predicted by Davidson et al.¹¹⁻¹³. Note that except in the limit of $I/I \rightarrow 0$, they predicted that there is a critical value β_c for the local plasma beta such that the lower-hybrid drift instability is completely stabilized for $\beta > \beta_c$.

IV. SATURATION MECHANISMS

We have studied several saturation mechanisms of the lower-hybrid drift instability in an uniform magnetic field. Simulation results show that the instability is stabilized by ion trapping when both the density gradient and the relative electron-ion drift velocity v_d are kept constant in time because of external circuits for example. It is found that the saturation level predicted by quasilinear theory^{7,8} is the saturation level of the most unstable mode via ion trapping. Allowing the electron cross-field drift velocity v_{th} to vary in time, the wave stops growing at a much lower level as the current relaxes.

A. Ion Trapping

In our simulations, the potential $\phi_k(t)$ was advanced by solving Eq. (16). Constant values of v_I , which drive the lower-hybrid drift instability, were studied first. In single mode simulation for the most unstable modes, there are oscillations of the wave energy at the trapping frequency ω (Fig. 5a and 5b) just after the time saturation and a vortex-like structure emerges in the ion phase space plots after saturation (Fig. 9a and 9b) for $v_I/v = 0.57$ and 0.85 . The end of wave growth was accomplished by ion trapping. All of the phase space pictures are presented in the wave frame, $x - v_{ph}t = \text{constant}$, where v_{ph} was calculated from linear theory. It is noted that vortices in Fig. 9a and 9b at small velocities are not due to the multibeam instability, because those vortices would appear at large velocities.

We compared these saturation levels with the quasilinear theory as given by Davidson⁸ under the assumption that the spectrum is strongly peaked about the fastest growing mode, for $v_I < v$. Fig. 10a shows that the simulation data are in agreement with the quasilinear saturation level ϵ_s given by his Eq. (48)

$$\epsilon_s = \frac{2}{45\sqrt{\pi}} \left[\frac{v_I}{\sqrt{2}v} \right]^5 \cdot \frac{nT}{1 + \omega_{pe}^2/\omega_{ci}^2} \quad (19)$$

There is a factor of $\sqrt{2}$ difference in v_I in our version of Davidson's equations because of our differing definition of T , $T = m_i v_i^2$.

It is necessary to explain why the simulations shows that nonlinear saturation was due to ion trapping but the saturation levels agreed with Davidson's quasilinear theory. In deriving the saturation level ϵ_s (Eq. 19), Davidson began with an energy conservation equation and the only real invocation of quasilinear theory seems to be the specification that saturation occurs when the distribution function has been "flattened" around the mode phase velocity. Such flattening could in principle be due to a variety of causes besides the usual quasilinear diffusion, for example, trapping. Equating the field energy to the ion kinetic energy change due to "flattening" gives his Eq. (46),

$$\left(1 + \frac{\omega_{pe}^2}{\omega_{ci}^2}\right) \int dk \left(1 + \frac{k^2}{k_{De}^2}\right) \epsilon_s(t \rightarrow \infty) = \frac{4}{45\sqrt{\pi}} \left[\frac{v_I}{\sqrt{2}v} \right]^5 nT \quad (20)$$

To calculate the left side of the above equation, Davidson assumed that the spectrum is sufficiently peaked about $k^* = k^*$ (the wavenumber corresponding to maximum growth for the initial equilibrium conditions) that $1 + k^2/k_m^2 \approx 2$ is a good approximation in the integrand in Eq. (20). This was equivalent to a single mode assumption. Eq. (19) was then obtained.

The trapping frequency is given by

$$\omega_{tr} = k_m \left[\frac{e\phi}{m} \right]^{1/2}, \quad (21)$$

where

$$\phi = \left[\frac{8\pi\epsilon_1}{k_m^2 V} \right]^{1/2}$$

is the electric potential. Using Eq. (19), we obtain

$$\omega_{tr} = (k_m v_e \omega_{ce})^{1/2} \left[\frac{4}{45\sqrt{\pi}} \right]^{1/4} \left[\frac{v_e}{\sqrt{2}v_{Te}} \right]^{3/4}. \quad (22)$$

Using γ from Eq. (9) at $k = k_m$, Eq. (22) can be rewritten as

$$\begin{aligned} \frac{\omega_{tr}}{\gamma_e} &= \left[\frac{4}{45\sqrt{\pi}} \right]^{1/4} \frac{8}{\sqrt{2}\pi} \left[\frac{\sqrt{2}v_e}{v_T} \right]^{3/4} \\ &= 1.975 \left[\frac{v_e}{v_T} \right]^{3/4}. \end{aligned} \quad (23)$$

When $v_e < v_{Te}$, the trapping frequency is larger than the growth rate and hence larger than the bandwidth $\Delta\omega \approx \gamma$ as well. Therefore, ion trapping will be the saturation mechanism when the fastest growing mode is dominant, and ϵ_1 in Eq. (19) will be the saturation level due to ion trapping. Comparison of Eq. (23) with the observed trapping frequencies (as in Fig. 11) indicates fairly good agreement for cases in which $v_e < v_{Te}$.

Finally, multi-mode simulations have been performed, i.e., all possible modes are excited at $t=0$. Typically, parameters used were the same as those for the single-mode run. The fastest growing mode tended to reach the same saturation level no matter whether only a single mode was kept or all modes were included in the simulations. In the wave frame of the most unstable mode, the ion phase space plot has a vortex formation about $v_x=0$ after saturation for $v_e/v_{Te}=0.57$ as shown in Fig. 12a. The length of the plasma was $L=2\pi$, and the number of

grids was $NG=64$. Furthermore, a dip appears at the approximate wave phase velocity in the ion distribution curve in Fig. 12b. The ion phase space and the distribution curve are presented in Figs. 13a and 13b for $v_I/v_e=0.85$. The corresponding ion phase space picture for $L=4\pi$, and $NG=128$ is given in Fig. 14, showing that trapping still occurred for a finer mode spacing, viz. when Δk was reduced to half, i.e., $\Delta k \lambda_D = 0.07$. Figs. 12, 13 and 14 show the dominant mode at saturation to be $k \lambda_D \approx 1/\sqrt{2}$, which is the fastest growing mode.

In general, trapping tends to flatten the local velocity distribution, centered on the wave phase velocity, over a small resonant range ($v_{ph} - v_{trap} < v_{ph} + v_{trap}$). From Eq. (8), the phase velocity of the lower-hybrid drift instability,

$$v_{ph} \equiv \frac{\omega}{k} = \frac{k^2}{k^2 + k_m^2} v_I, \quad (24)$$

are well separated for different mode numbers k , and are much less than the ion thermal velocity for $v_I \ll v_e$. Therefore, each mode traps independently and flattens a different fraction of the ion velocity distribution for the resonant velocity range $0 < v < v_{ph}$. Hence, Eq. (20) is replaced by

$$\left(1 + \frac{\omega_{pe}^2}{\omega_{pi}^2}\right) \left(\frac{\epsilon_k}{nT}\right)_{sat} = \frac{1}{45\sqrt{2}\pi} \cdot \frac{1}{1 + k^2/k_m^2} \cdot \left(\frac{v_I}{v_e}\right)^5 \quad (25)$$

for the saturation level of each discrete mode due to ion trapping. Comparison of the simulation saturation field energy spectrum with Eq. (25) is given in Figs. 15a and 15b for single-mode and many-mode runs, respectively. The co-existence of the multibeam modes causes the large error bars shown in Fig. 15. However there still is fairly good agreement between simulation and theory. Both simulation data and the theoretical curves for small k/k_m are not plotted because, following Eq. (8), the real part of mode frequency is less than the ion cyclotron frequency for small k/k_m , and the lower-hybrid drift mode turns into an ion drift cyclotron mode; our theory and simulations do not extend into that region.

Trapping was also observed by Winske and Liewer in their 2d particle simulations with v_I large than v_e . For $v_I \gg v_e$, they estimated that ion trapping required

$$\left(\frac{e\phi}{T}\right)_{sat} < \left(1 + \frac{v_{th}^2}{v_I^2}\right) \quad (26)$$

anomalous transport.

For time $t = n\Delta t > nth\Delta t$, we use a predictor-corrector scheme. We define predicted quantities $v_{dk,p}^n$ and T_{ep}^n as

$$v_{dk,p}^n = v_{dk,p}^{n-1} \quad \text{and} \quad T_{ep}^n = T_{ep}^{n-1}. \quad (29)$$

By solving Eq. (15), we obtain the predicted electric field E_p^n and the field energy. We then advance the particle velocities from $v^{n-1/2}$ to $v_p^{n+1/2}$ by using E_p^n and calculate the predicted total ion kinetic energy W_p^n and ion momentum P_p^n ,

$$W_p^n = m_i \sum_{j=1}^N v_j^{n-1/2} v_j^{n+1/2} \quad (30)$$

$$P_p^n = (P_p^{n-1/2} + P_p^{n+1/2})/2 \quad (31)$$

where $P_p^{n+1/2} = m \sum_{j=1}^N v_j^{n+1/2}$. Now we define the corrector portion of the algorithm. Eq. (27) yields

$$v_{dk}^n = v_{dk}^n + (P_p^n - P_i^n)/nm_i \quad (32)$$

We substitute v_{dk}^n into Eq. (28) and obtain

$$\frac{nT_e^n}{2} = \frac{nT_e^n}{2} + W_p^n + \epsilon^n + \frac{nm_i v_{dk}^{n2}}{2} - W_p^n - \epsilon_p^n - \frac{nm_e v_{dk}^{n2}}{2}. \quad (33)$$

We then substitute v_{dk}^n and T_e^n into Eq. (15) and solve for the electric field E^n and the field energy ϵ^n .

Using this method, the simulations agree with the linear theory at small wave amplitudes for various values of nth . Fig. 17 shows a field energy history plot using time varying v_{dk} and T_e and $v_i/v_e \approx 0.85$ and $nth\Delta t = 100$. (The results are not sensitive to making $nth\Delta t$ smaller.) As compared to Fig. 5b, the instability now saturates at a much lower level because of the current relaxation that occurs. By assuming that the system is stabilized via current relaxation, the saturation level of the fluctuation spectrum was estimated by Davidson et al.^{7,8} at

$$\epsilon_s = \frac{1}{2} \frac{nm_e v_{dk}^2/2}{2(1 + \omega_{pe}^2/\omega_{ci}^2)}; \quad (34)$$

the corresponding changes in the ion temperature and electron temperature after saturation were given by

$$\frac{\Delta I}{I} \approx 2 \left(1 + \frac{\omega_{pi}^2}{\omega_{ci}^2} \right) \cdot \frac{\epsilon_y}{nT} \quad (35)$$

and

$$\frac{\Delta T_i}{T_i} \approx \frac{\omega_{pi}^2}{\omega_{ci}^2} \cdot \frac{\epsilon_y}{nT} \quad (36)$$

for $T_i/T \ll 1$ and $v_d/v_{th} \ll 1$. For our simulation parameters, $\Delta T_i/T$ and $\Delta I/I$ are about 10^{-5} , and are too small to be observed. Comparison of simulation results for time varying v_{th} and T with that for constant v_{th} and T is given in Fig 10, showing that current relaxation stabilizes the instability when v_{th} and T are dynamic; otherwise, ion trapping stabilizes the instability. For cases in which $v_d \ll v_{th}$ and v_{th} is allowed to relax in time, the saturation level of ϵ_y/nT is so small that it is masked by the thermal fluctuations, whose levels are equal to $\approx 10^{-5}$ in our simulations. Thus, no data appears on the curve labeled (b) in Fig. 10 for $v_d/v_{th} < 0.8$. Note that in a finite beta plasma, the particle drifts and magnetic field are coupled and, consequently, the anomalous dissipation of the particle drift energy and magnetic energy are also linked. Therefore, the magnetic field effectively acts as a free energy source to drive the instability, and current relaxation will not occur¹⁸.

V. CONCLUSIONS

One-dimensional particle-hybrid simulations of the lower-hybrid drift instability in the low drift velocity regime have been described in this paper. At small amplitudes, the simulations agree very well with the linear theory. Saturation mechanisms have been investigated for cross-field drift velocities less than the ion thermal velocity. It has been shown that the lower-hybrid drift instability is stabilized by ion trapping if cross-field drift velocities are kept constant in time because of external circuits, for example. An analytic formula, which agrees very well with simulation results, for the saturated field energy spectrum in k space for ion trapping has been given in Sec. III A. If cross-field drift velocities are allowed to vary in time, growth of the instability will be stabilized through current relaxation.

ACKNOWLEDGMENTS

We are greatly indebted to Dr. B. I. Cohen for his encouragement, numerous helpful discussions, suggestions and a critical reading of the manuscript. We would also like to thank Dr. W. Nevins for his helpful conversations and interest in our efforts.

This research was supported by the Office of Naval Research Contract No. N00014-77-C-0578.

REFERENCES

1. N. A. Krall and P. C. Tiewer, "Low-Frequency Instabilities in Magnetic Pulses", Phys. Rev. A **4**, 2094 (1971).
2. M. Keilhacker, M. Kornherr, H. Niedermeyer, F. Soldner, and K.-H. Steuer, Phys. Rev. Lett. **32**, 1044 (1974).
3. K. E. McKenna, R. Kristal, and E. E. Zimmermann, "Radial Plasma Structure during a Theta-Pinch Implosion: Flute Instabilities", Phys. Fluids **18**, 1371 (1975).
4. D. B. Batchelor and R. C. Davidson, "Nonlocal Analysis of the Lower-Hybrid-Drift Instability in Theta-Pinch Plasmas", Phys. Fluids **19**, 882 (1976).
5. D. Winske and P. C. Tiewer, "Particle Simulation Studies of the Lower Hybrid Drift Instability", Phys. Fluids **21**, 1017 (1978).
6. N. E. Gladd, Plasma Phys. **18**, 27 (1976).
7. R. C. Davidson and N. E. Gladd, "Anomalous Transport Properties Associated with the Lower-Hybrid-Drift Instability", Phys. Fluids **18**, 1327 (1975).
8. R. C. Davidson, "Quasi-linear Stabilization of the Lower-Hybrid-Drift Instability", Phys. Fluids **21**, 1375 (1978).
9. J. D. Huba and K. Papadopoulos, "Nonlinear Stabilization of the Lower-Hybrid-Drift Instability by Electron Resonance Broadening", Phys. Fluids **21**, 121 (1978).
10. C. E. Dum and E. H. Dupree, "Nonlinear Stabilization of High-Frequency Instabilities in a Magnetic Field", Phys. Fluids **12**, 2064 (1970).
11. R. C. Davidson, N. E. Gladd, C. S. Wu, and J. D. Huba, "Influence of *Finite- β* Effects on the Lower-Hybrid-Drift Instability in Post-Implosion θ Pinches", Phys. Rev. Lett. **37**,

750 (1976).

12. R. C. Davidson, N. T. Gladd, C. S. Wu, and J. D. Huba, "Effects of Finite Plasma Beta on the Lower-Hybrid-Drift Instability", Phys. Fluids **20**, 301 (1977).
13. R. C. Davidson, N. T. Gladd and Y. Goren, "Influence of magnetic Shear on the Lower-Hybrid-Drift Instability in Toroidal Reversed-Field Pinches", Phys. Fluids **21**, 992 (1978).
14. B. I. Cohen and N. Maron, "Simulation of Drift-Cone Modes", Phys. Fluids **23**, 974 (1980).
15. B. I. Cohen, N. Maron and G. R. Smith, "Some Nonlinear Properties of Drift Cyclotron Modes", LLL report UCRL-84320 (1980), to be published in Phys. Fluids.
16. J. M. Dawson, "Plasma Oscillations of a Large Number of Electron Beams", Phys. Rev. **118**, 381 (1960).
17. H. S. Au-Yeung and A. Friedman, "SOLVER: An Analytic Function Root Solving and Plotting Package", U. C. Berkeley Electronics Research Laboratory Report No. UCB/ERL M79/55 (1979).
18. J. D. Huba, J. E. Drake and N. T. Gladd, "Diffusion and Magnetic Energy Dissipation in Field Reversed Plasma", Sherwood Theory Meeting, Tucson, Arizona (1980).

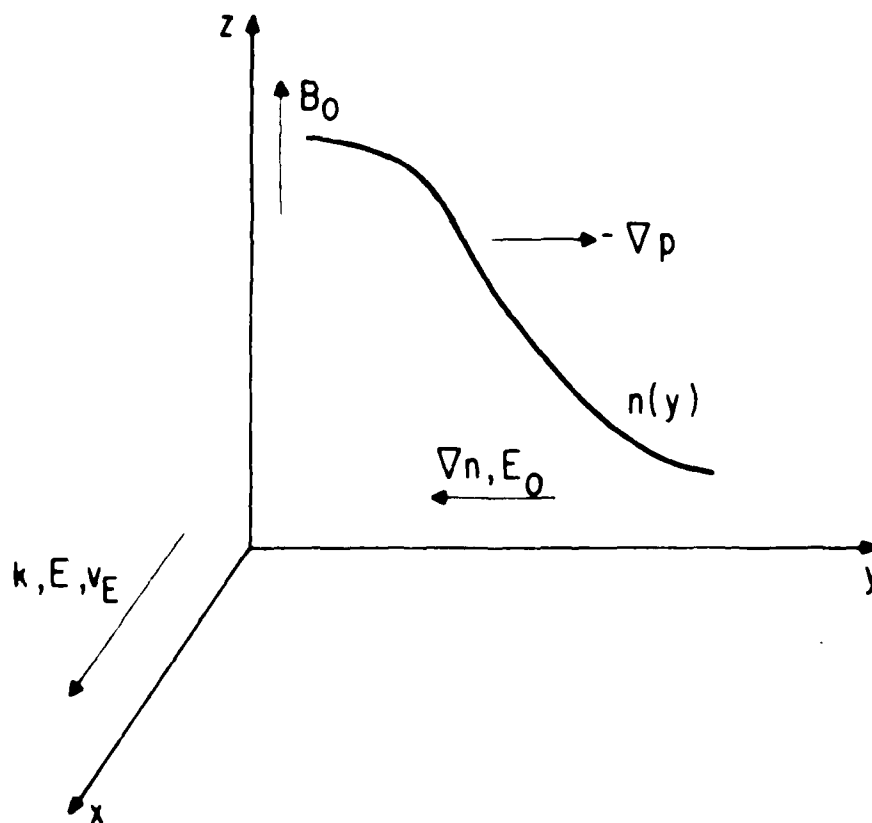


Fig. 1 Slab coordinates for lower-hybrid drift instability. one dimensional simulations were performed in the x direction only.

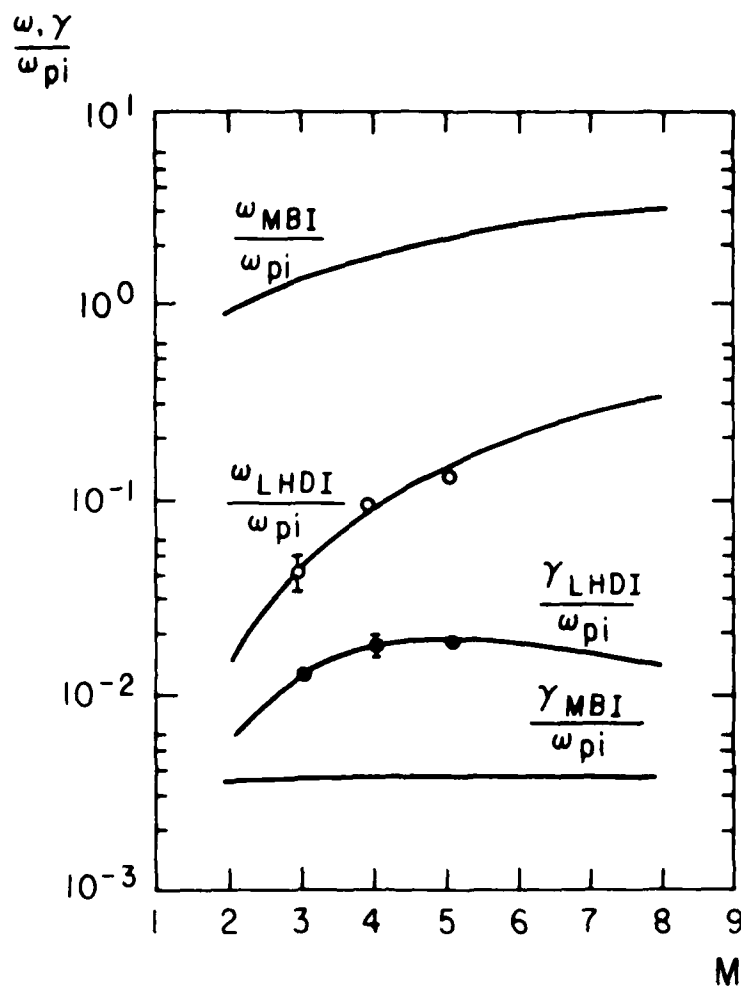


Fig. 2 Dispersion curves for the lower-hybrid drift mode and the fastest growing multi-beaming mode for: $N=N_e=16384$, $m_e/m_i=1600$, $\omega_{ce}/\omega_{ci}=1$, $\lambda_D/\Delta x=1.44$, $v_i/v_e=0.424263$, $T_e=0$, $L_u/L_R=0$, and $L_u/L_f=0$. Simulation results are denoted by circles ($\omega_{LHDI}/\omega_{pi}$) and dots ($\gamma_{LHDI}/\omega_{pi}$). $M=kL/2\pi$ is the mode number

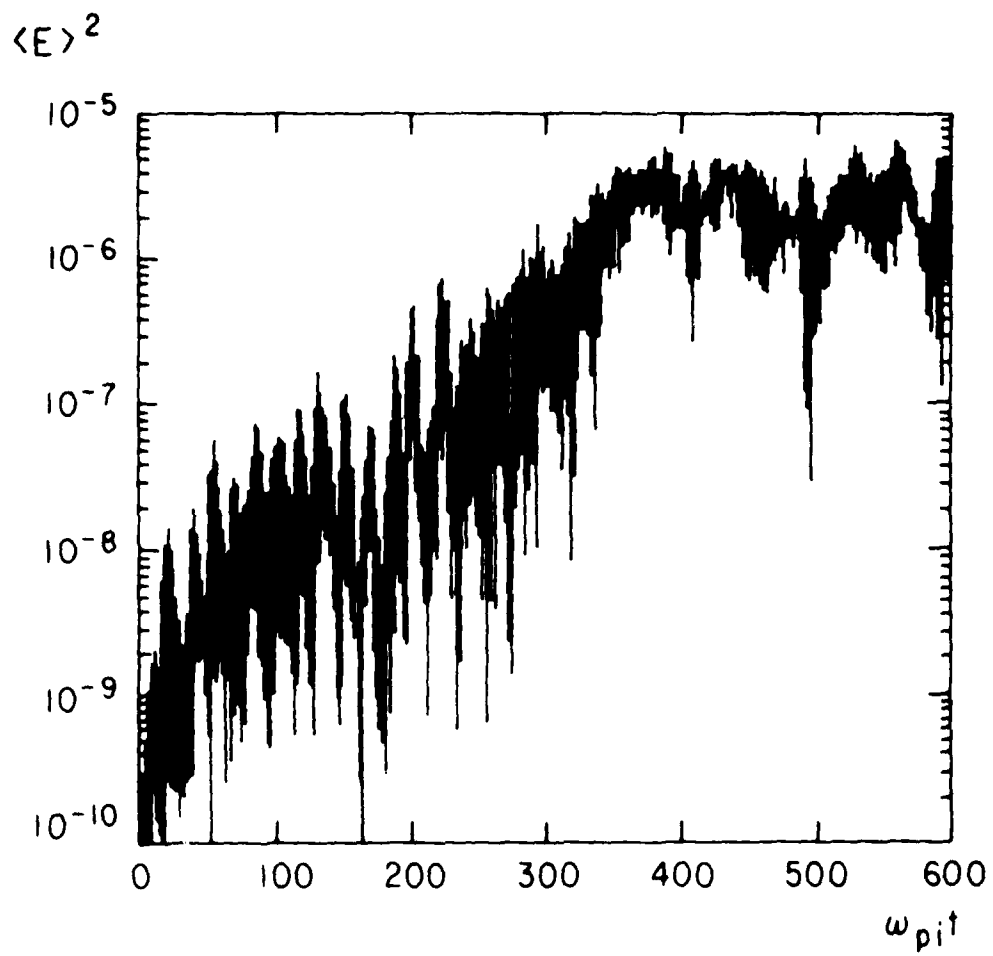


Fig. 3 Electric field energy versus time for simulation with $M=5$, parameters of Fig. 2

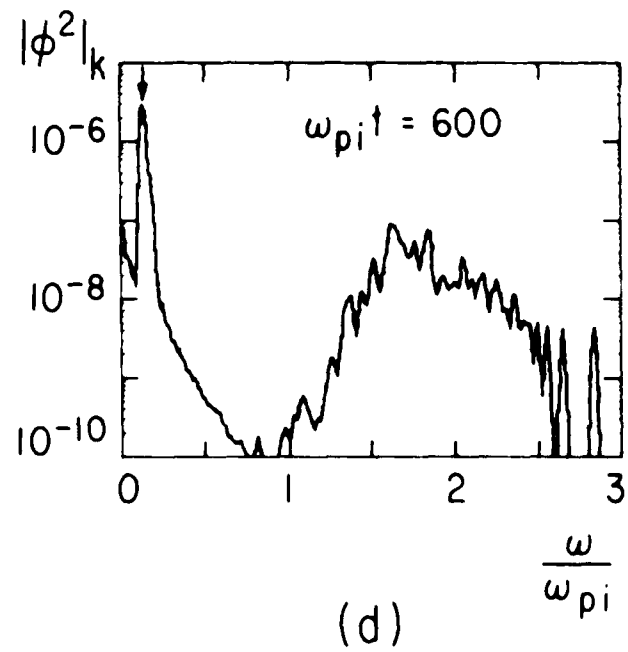
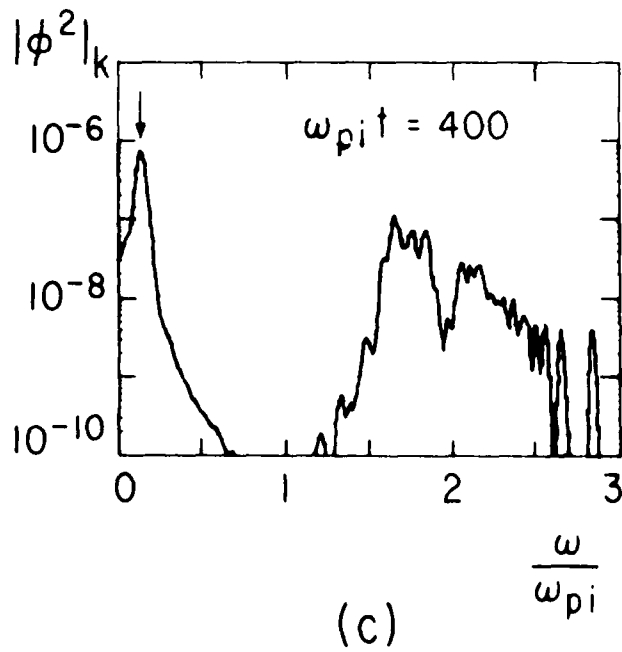
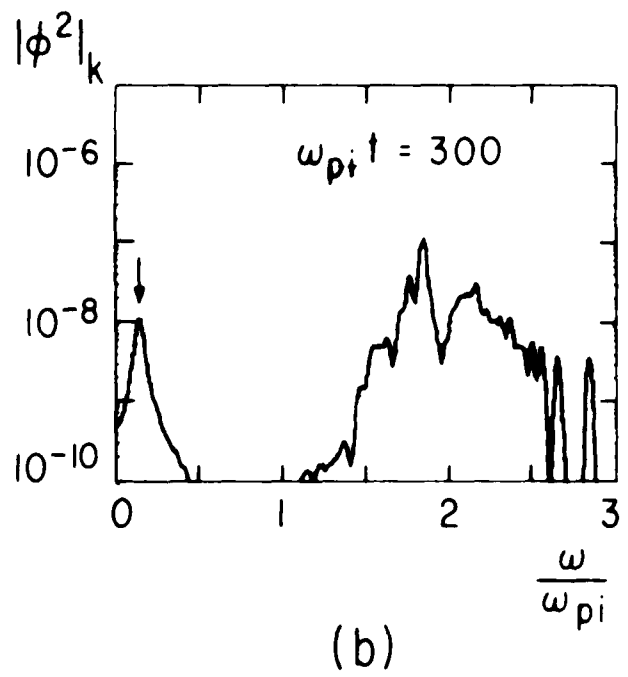
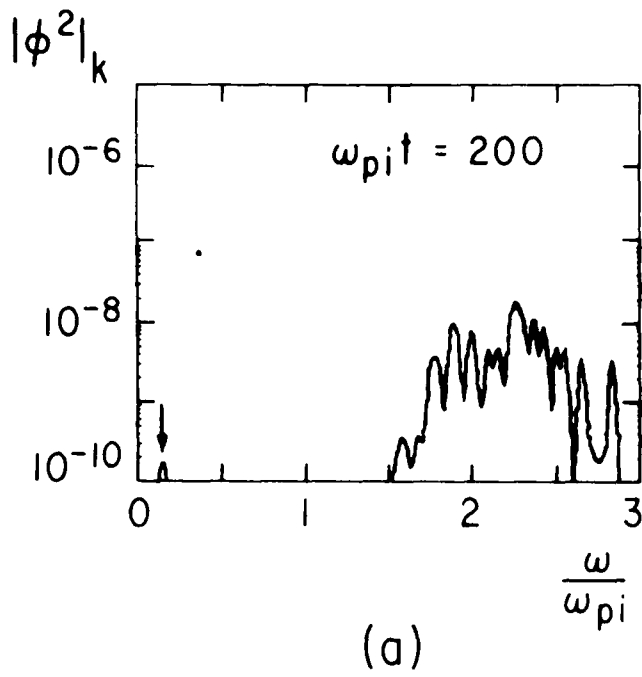


Fig. 4 Power spectrum $|\phi^2|_k(\omega)$ at (a) $\omega_p T=200$, (b) $\omega_p T=300$, (c) $\omega_p T=400$, and (d) $\omega_p T=600$ for $M \equiv kL/2\pi=5$, parameters of Fig. 2. The sharp peak at $\omega/\omega_p \approx 0.136$ corresponds to the lower-hybrid drift instability.

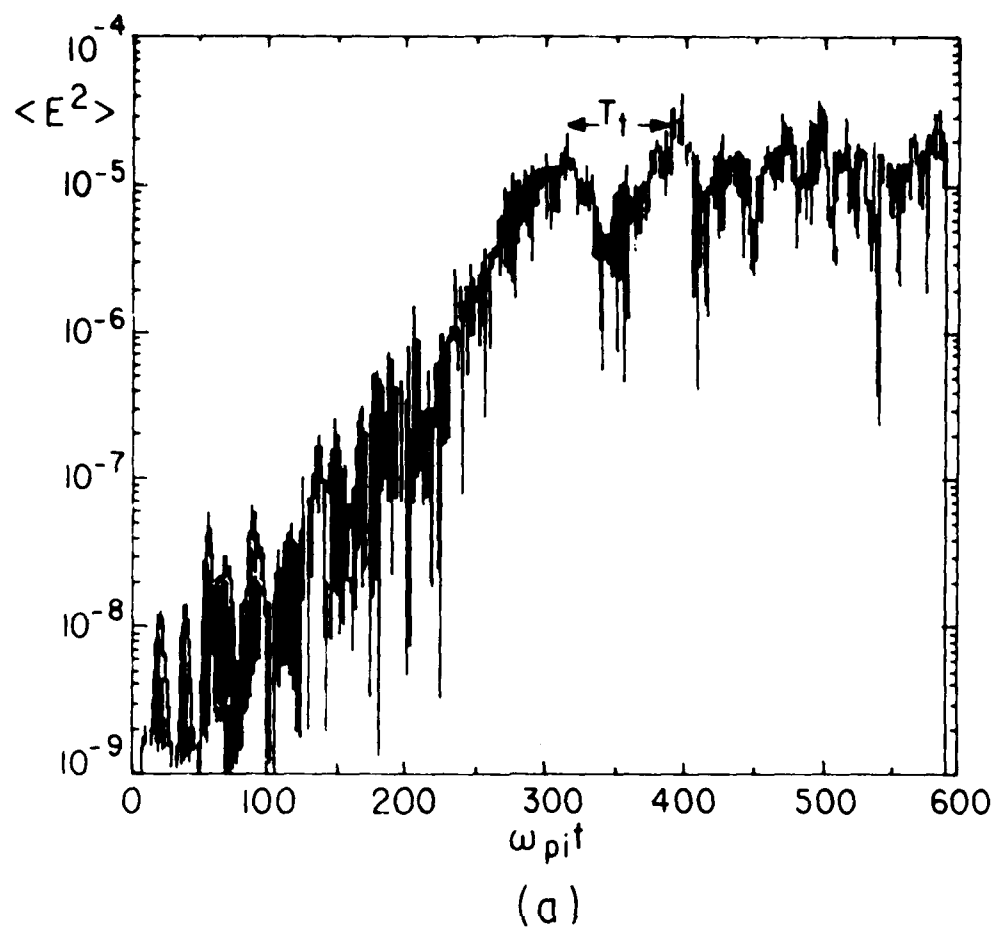
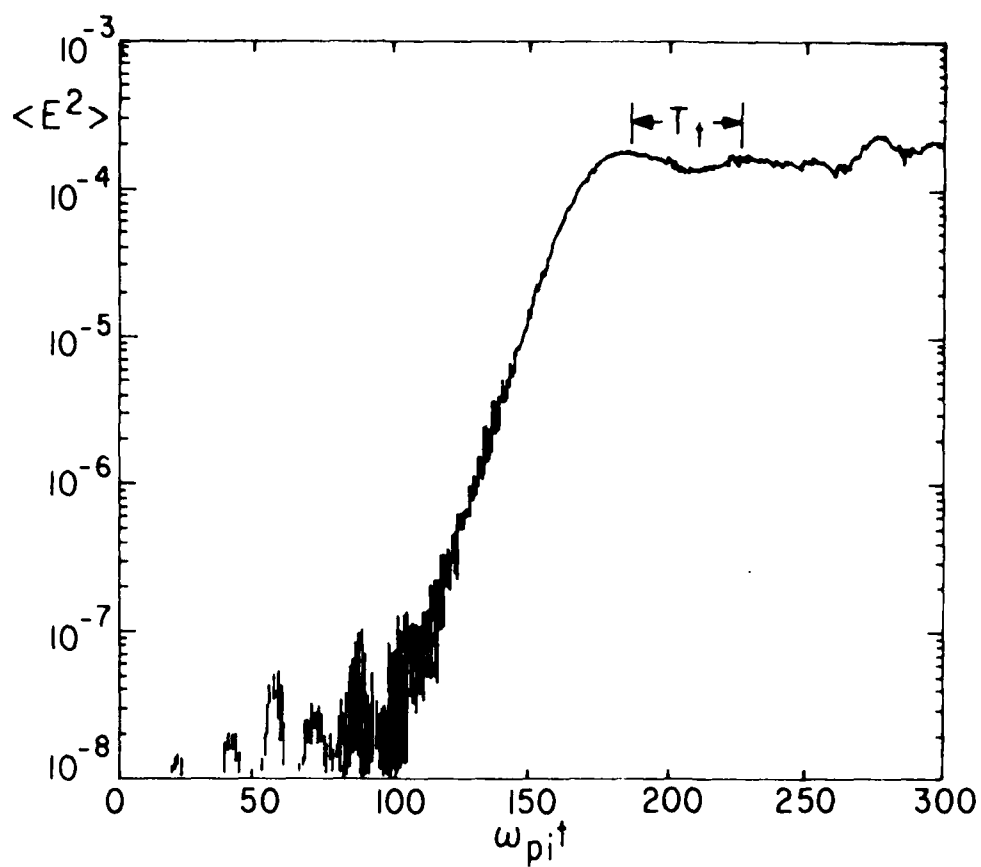


Fig. 5 Electric field energy history plots for parameters of Fig. 2, except for (a) $v_f/v_i = 0.57$: the high frequencies are due to the multibeam instability and low frequency is due to the LHDI, and (b) $v_f/v_i = 0.85$: here the multibeaming effects are much smaller at saturation, which is much higher than in (a).



(b)

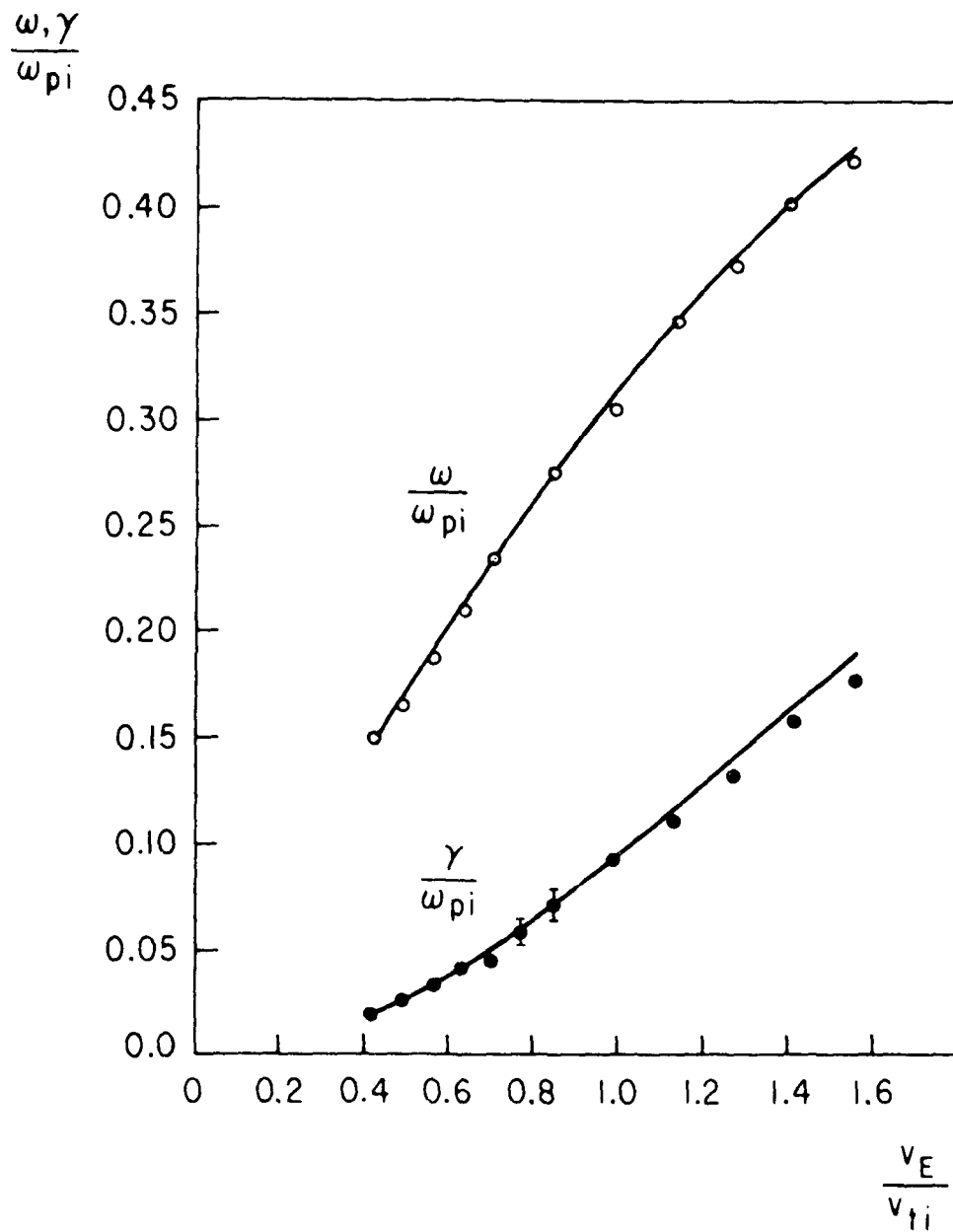


Fig. 6 Complex frequency versus v_E/v_{ti} for parameters Fig. 2. Simulation data are shown by circles (ω/ω_p) and dots (γ/ω_p). The solid curves represent the LHDI dispersion relation of Eq. (18).

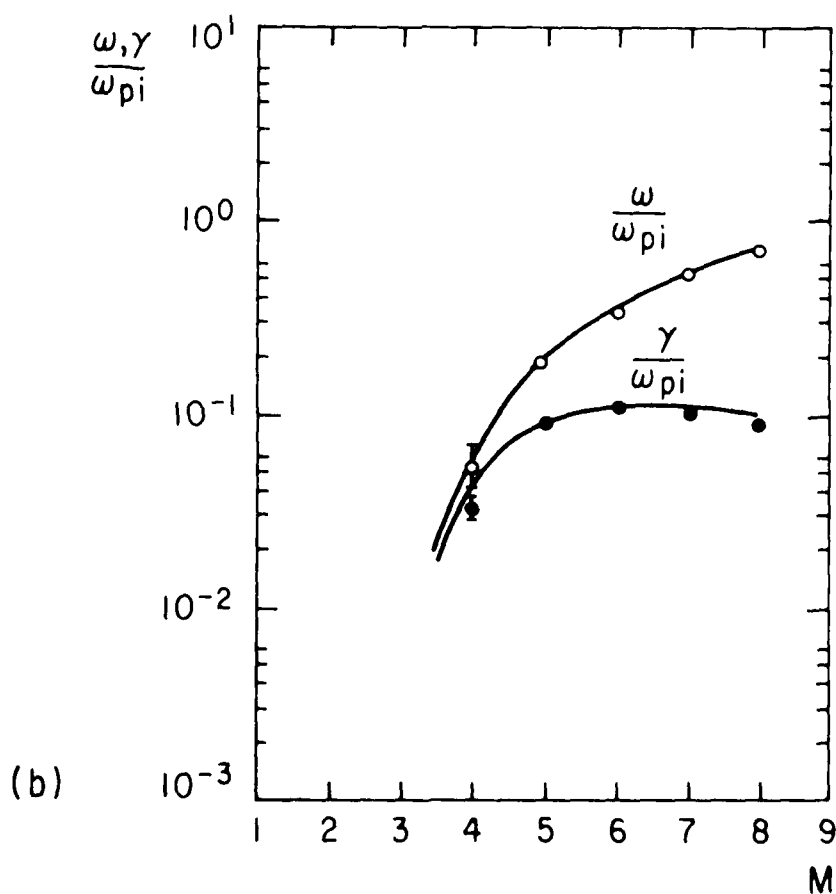
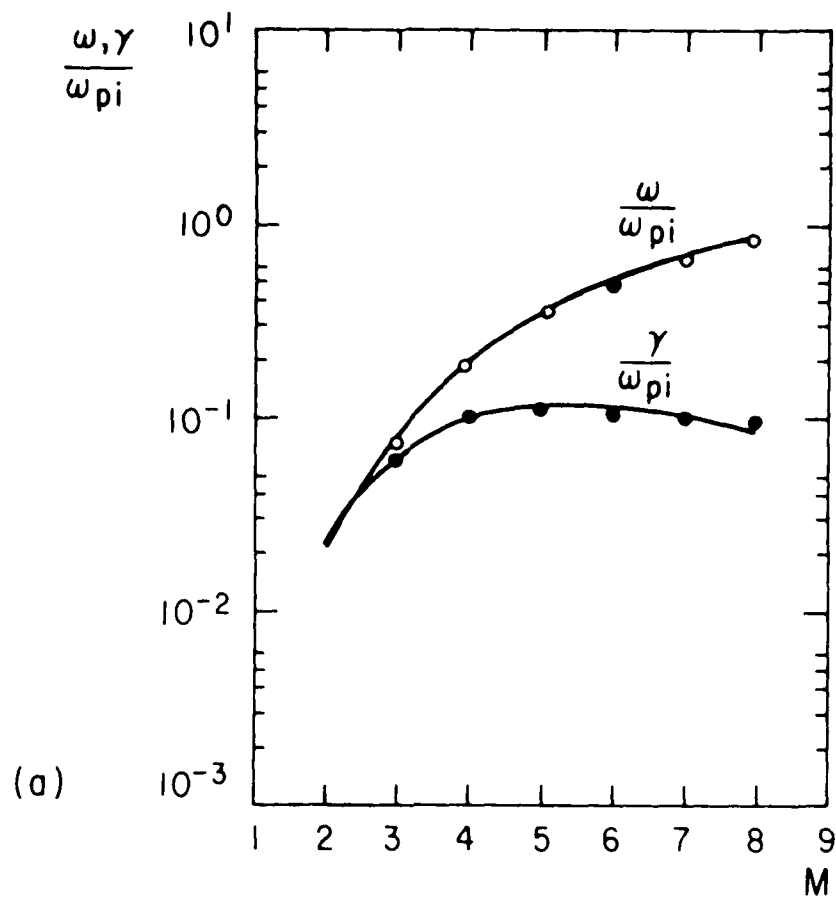


Fig. 7 Lower-hybrid drift dispersion curves for parameters of Fig. 2, except $v_i/v = 1.1314$.

(a) $L_z/L_R=0$, and (b) $L_z/L_R=-0.40$. The curves are from Eq. (18).

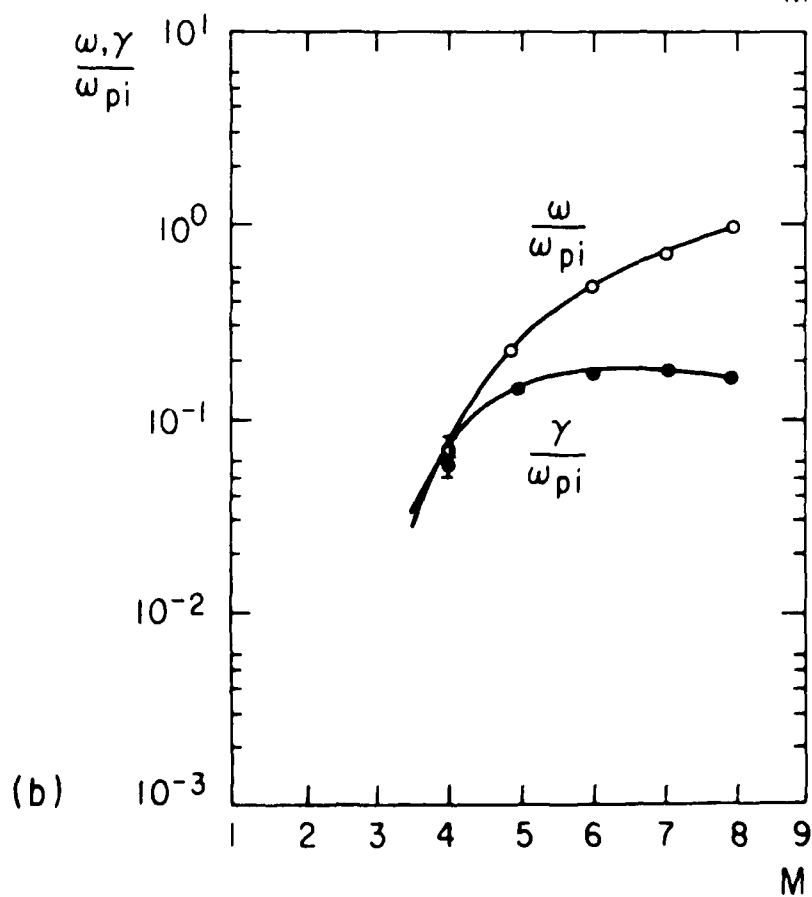
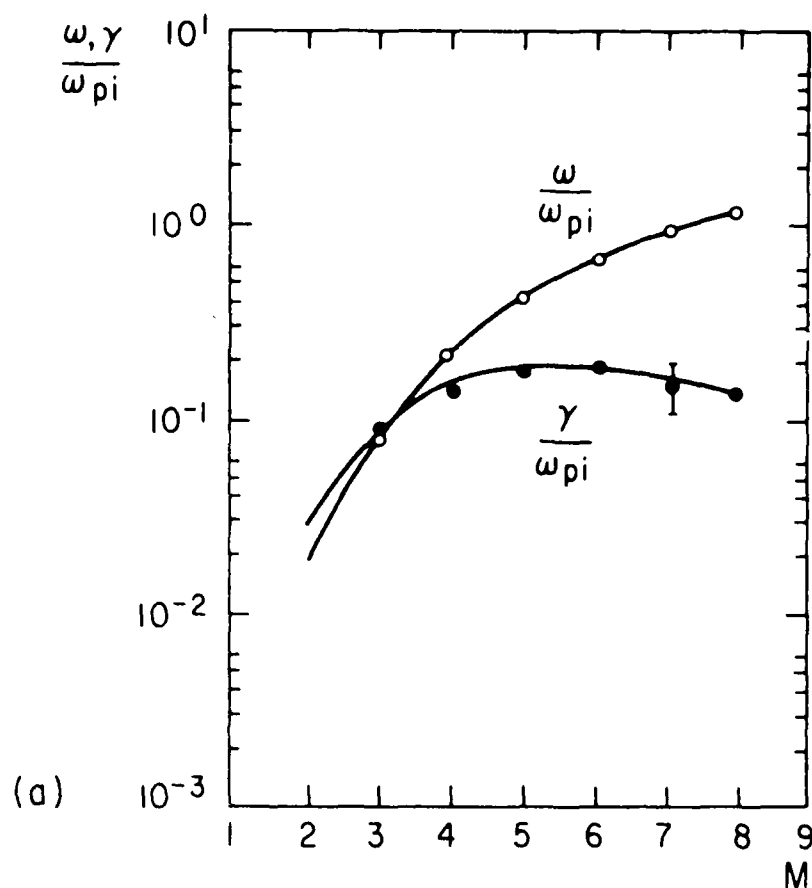


Fig. 8 Lower-hybrid drift dispersion curves for $v_i/v_e = 1.5556$, (a) $L_{\perp}/L_{\parallel} = 0$, and (b) $L_{\perp}/L_{\parallel} = -0.36$.

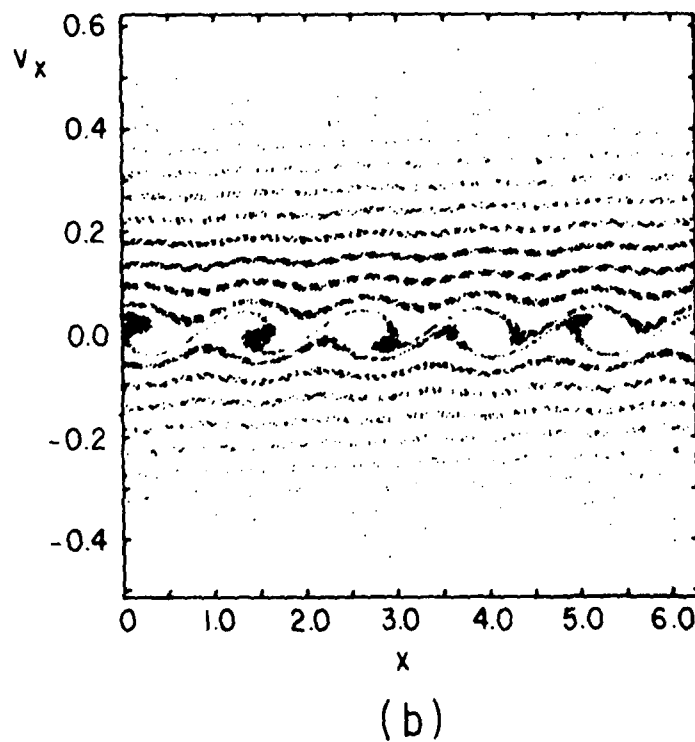
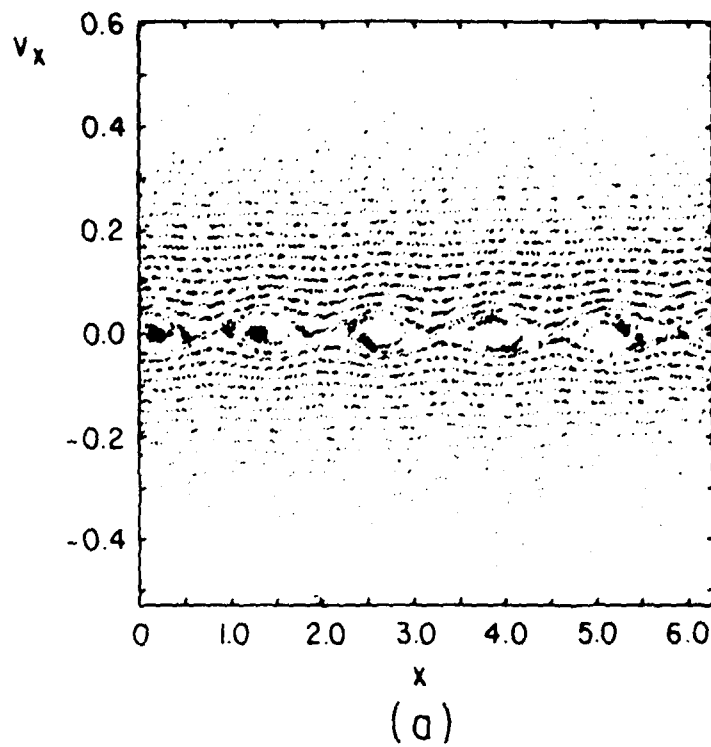


Fig. 9 Ion phase space pictures in the (x, v_x) wave frames after saturation for $k\lambda_D = 1/\sqrt{2}$. (a) $v_i/v_e = 0.57$, and (b) $v_i/v_e = 0.85$. The appearance of beams in ion phase space is because that only one of every 5 particles was plotted. The space between beams is filled by the four missing particles.

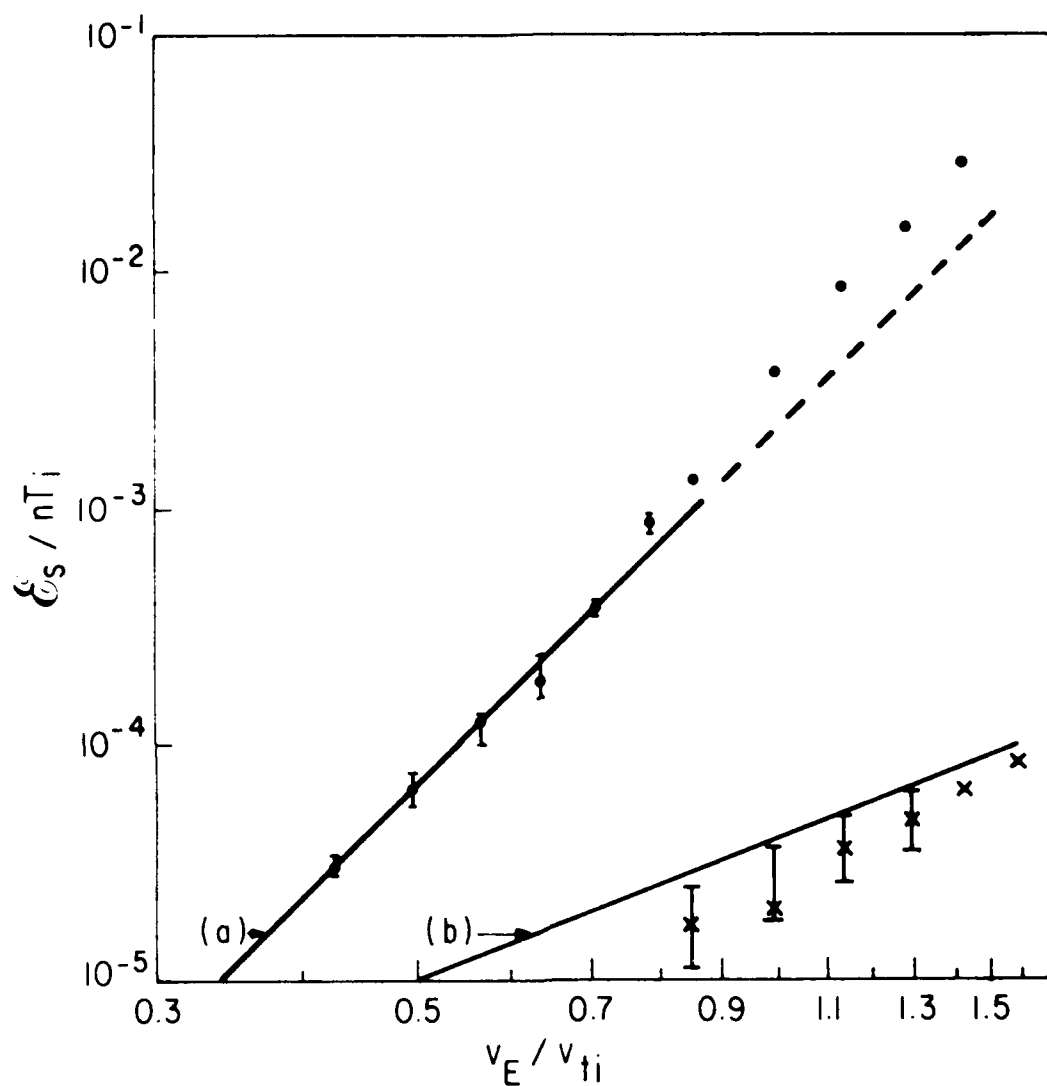


Fig. 10 Comparison of saturation field energies as functions of v_E/v_{ti} . (a) For constant v_{th} and T_e , the lower-hybrid drift instability is saturated by ion trapping. (b) For time varying v_{th} and T_e , saturation of the instability is achieved via current relaxation. The simulation data (dots in (a) and crosses in (b)) are in better agreement with the theory in (a) than in (b).

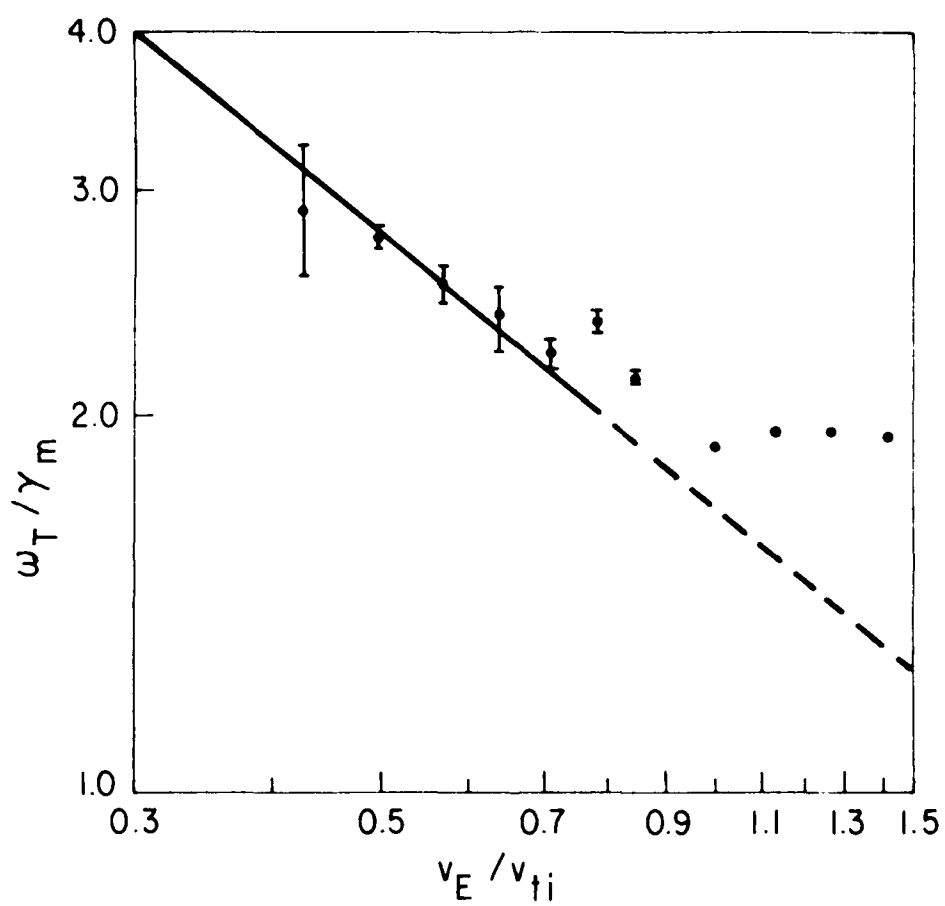
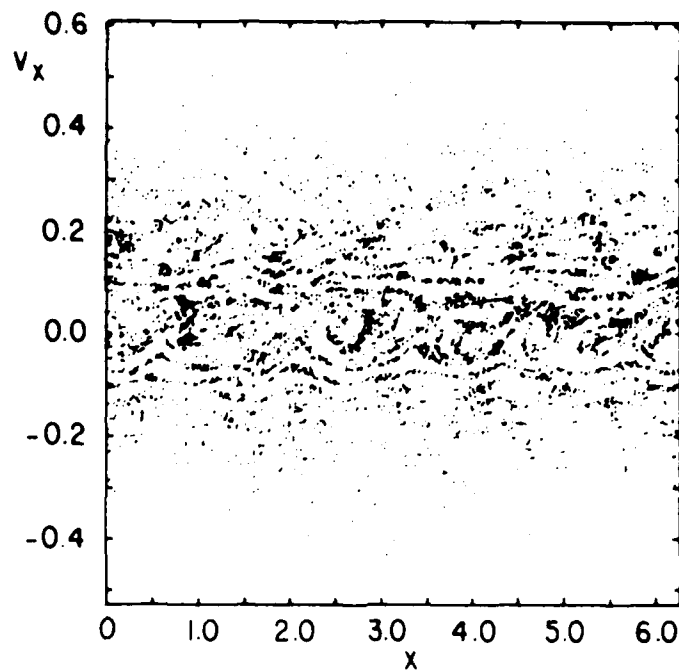
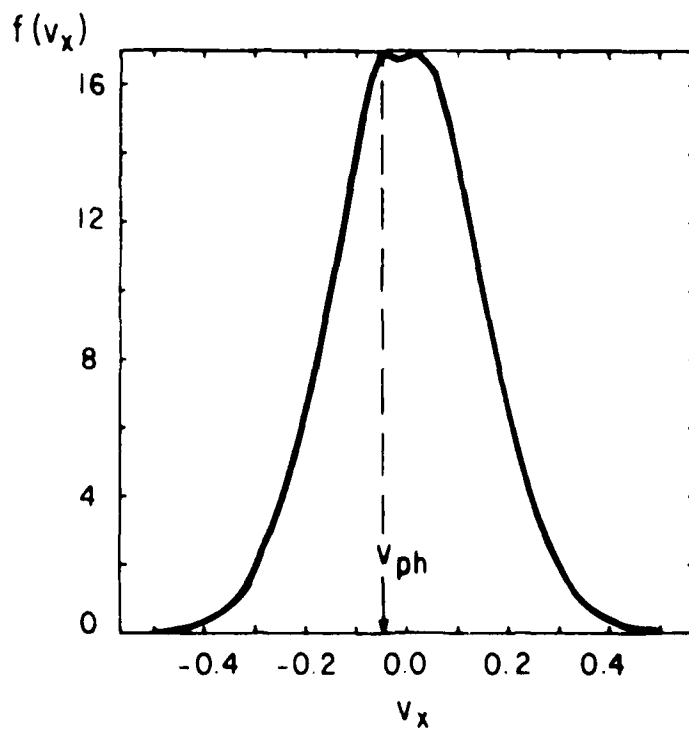


Fig. 11 Comparison of simulation trapping frequencies (single-mode runs) with ion trapping theory, Eq. (23). $\omega_f = 2\pi/T_f$ as shown in Fig. 5a,b.

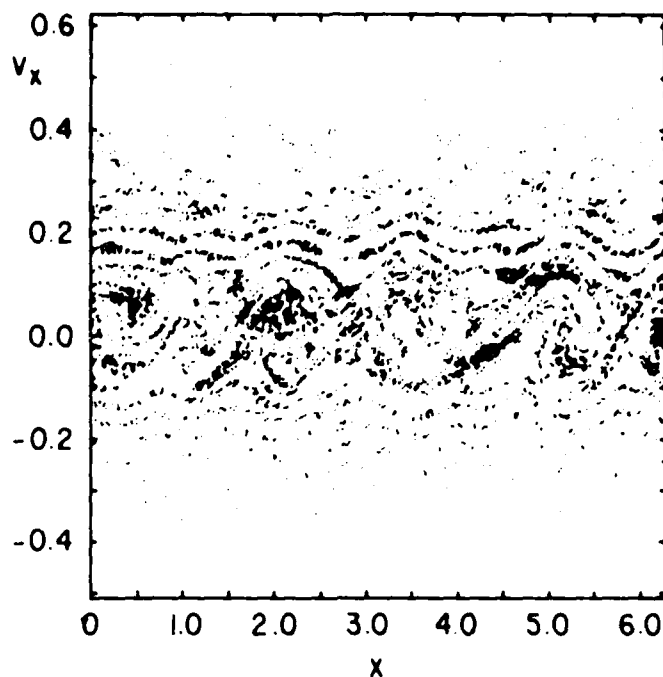


(a)

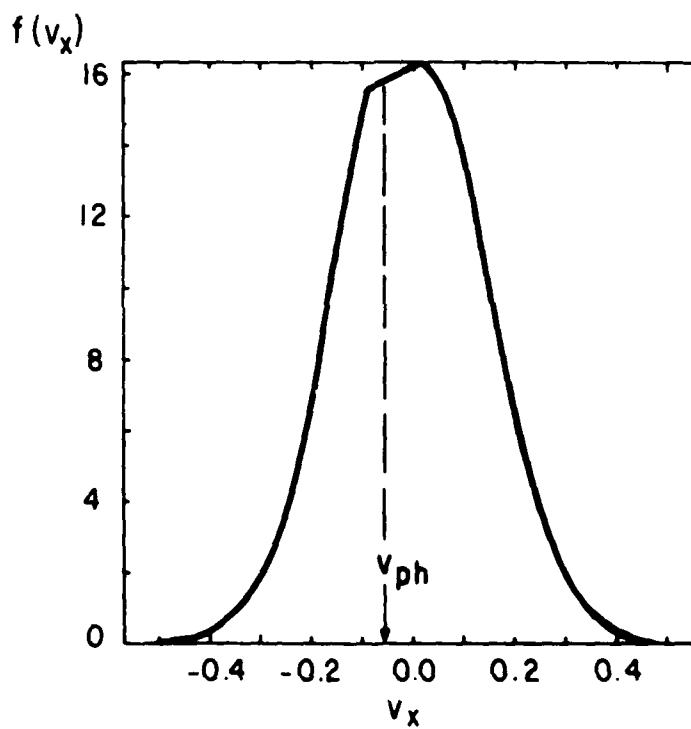


(b)

Fig. 12 Simulation (many-mode runs) of LHDI with parameters of Fig. 5a. Displayed are (a) the phase space in the wave frame of the most unstable mode, and (b) the ion velocity distribution function after saturation. v_{ph} is the phase velocity of the most unstable mode.



(a)



(b)

Fig. 13 Simulation (many-mode runs) of LHDI with parameters of Fig. 5b. Displayed are

(a) the phase space in the wave frame of the most unstable mode, and (b) the ion velocity distribution function after saturation. v_{ph} is the phase velocity of the most unstable mode.

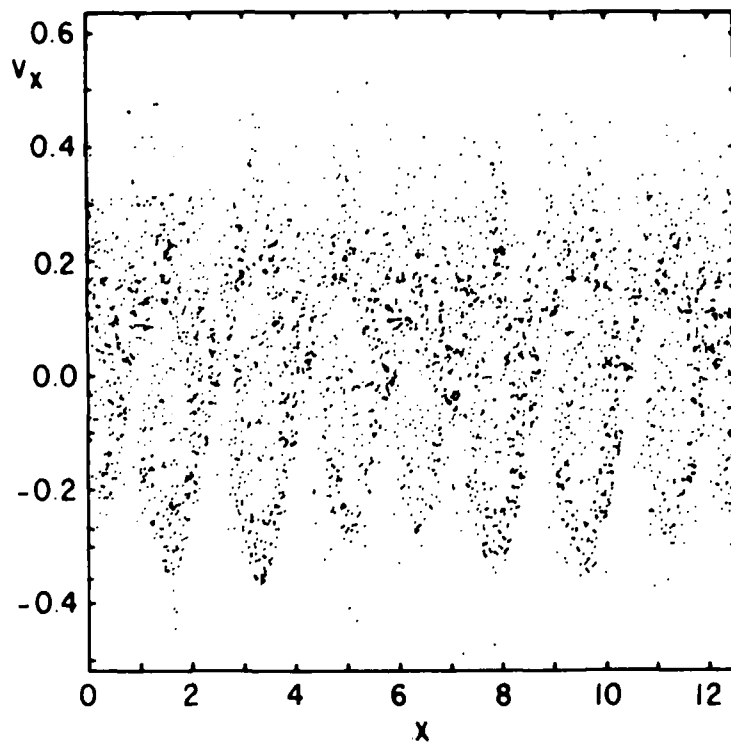


Fig. 14 The ion phase space in the most unstable mode frame after the saturation as $v_i/v_e=0.85$, and $\Delta k \lambda_D=0.0707$ (i.e., Δk half that of Fig. 13, but L twice that, so the dominant mode has the same wavelength).

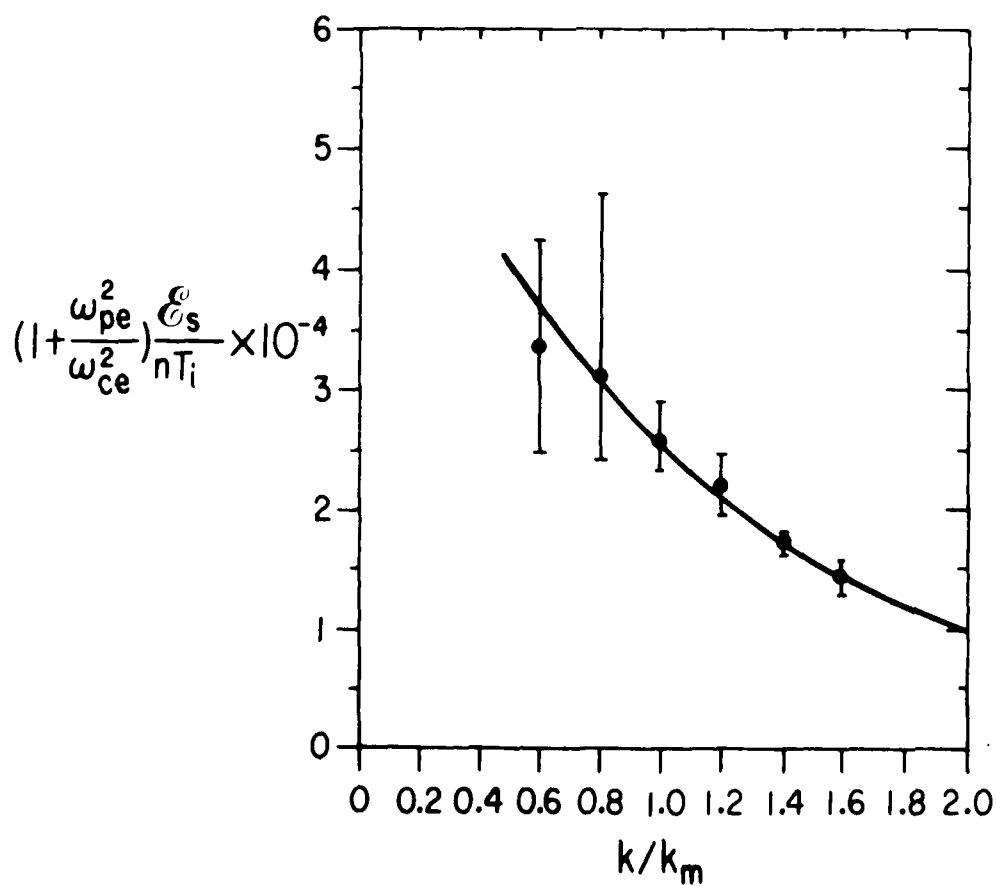
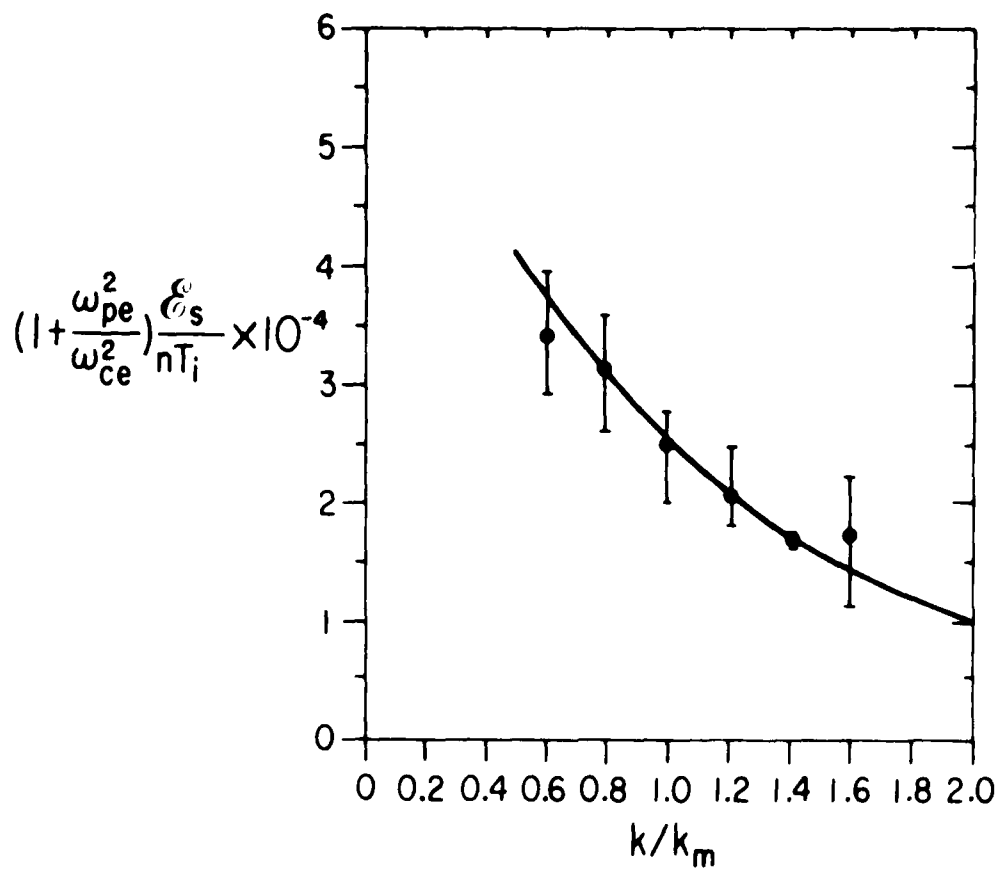


Fig. 15 The mode energy spectrum results for ion trapping versus k/k_m . Comparison of Eq. (25) with single-mode simulations is given in (a), and with many-mode simulations is in (b).

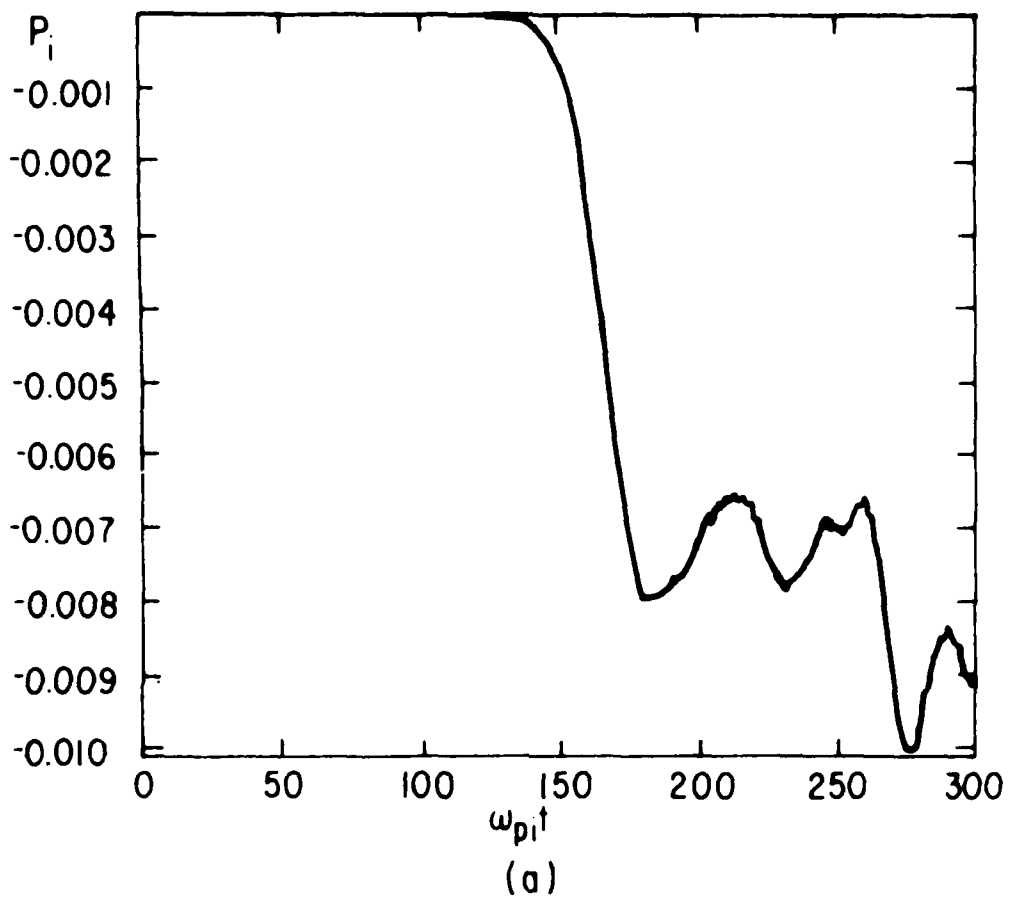
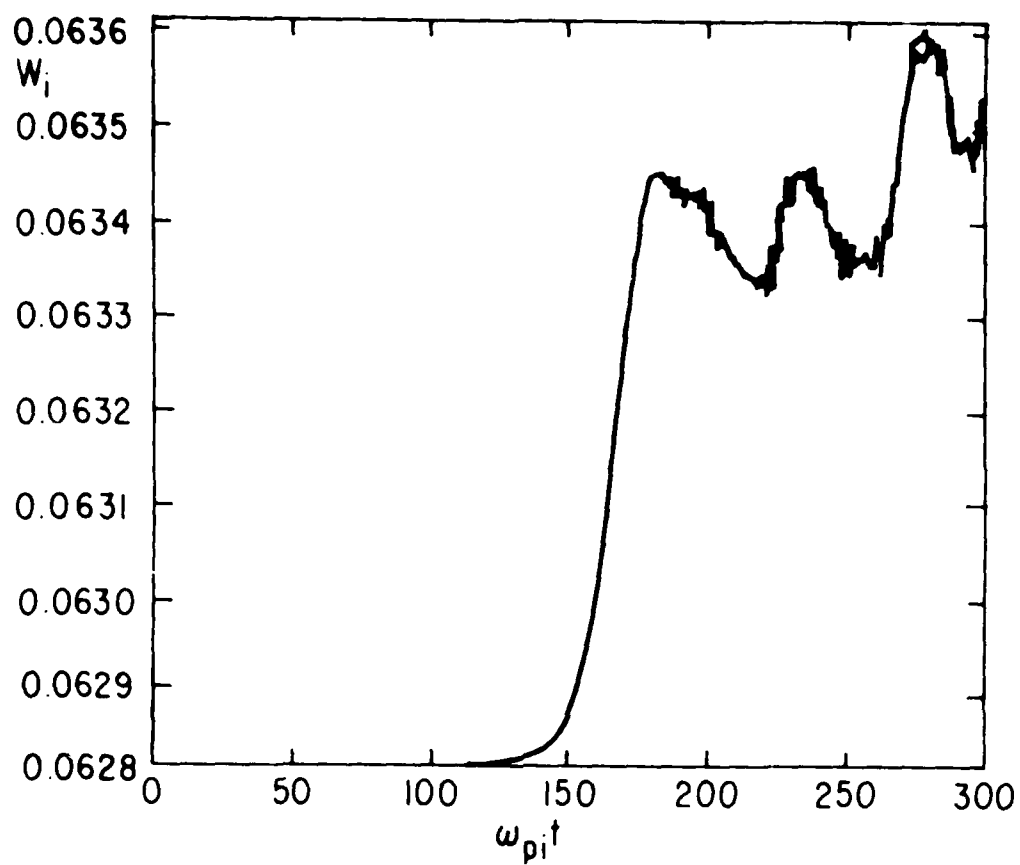


Fig. 16 History plots of (a) the total ion momentum and (b) ion kinetic energy for parameters of Fig. 5a, with no relaxation.



(b)

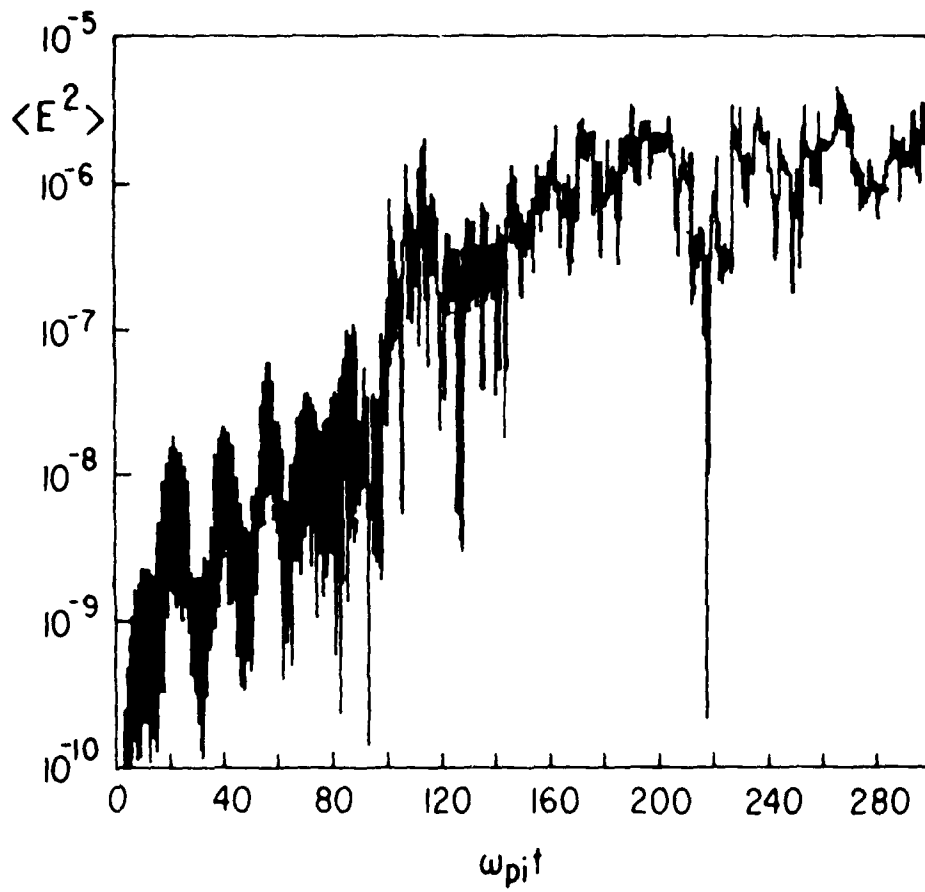


Fig. 17 Electric field energy history plots for time varying v_{th} and T_e ($n\theta\Delta t=100$), for parameters of Fig. 16.

